5-2018

Surface Area and Electrocatalytic Properties of FeNi Nanoparticles for the Oxygen Evolution Reaction (OER)

James Burrow

Surface Area and Electrocatalytic Properties of FeNi Nanoparticles for the Oxygen Evolution Reaction (OER)

A Study of the Effects of the Stabilizing Ligand PVP on the Physical and Electrochemical Properties of Alloy and Core Shell NPs

Author: James Burrow

Advisor: Dr. Lauren F. Greenlee

Ralph E. Martin Department of Chemical Engineering

University of Arkansas

Fayetteville, AR

Spring 2018

Abstract

Iron-nickel bimetallic electrocatalysts have recently emerged as some of the best candidates for the oxygen evolution reaction (OER) in alkaline electrolyte. Understanding the effects of composition and morphology of iron-nickel nanoparticles is crucial for optimization and enhanced electrocatalyst performance. Both physical surface area and electrochemical surface area (ECSA) are functions of morphology. In this study, four different iron-nickel nanoparticle catalysts were synthesized. The catalysts were varied based on morphology (alloy versus core-shell) and composition (low, medium, and high stabilizer concentration). Brunauer-Emmett-Teller (BET) surface area analysis was conducted on three of the synthesized iron-nickel nanoparticles using a physisorption analyzer while electrochemical impedance spectroscopy (EIS) was employed to quantify the ECSA by capacitance. Comparison of ECSA and BET results to electrocatalyst overpotential suggests both available surface area and nanoparticle morphology play roles in electrocatalytic activity. Additionally, compositional analysis by inductively coupled plasma mass spectroscopy (ICP-MS) suggests final nanoparticle composition is dependent on amount of stabilizing ligand added, with lower stabilizer concentrations resulting in less overall metal incorporation and larger deviations from theoretical compositions. This project holds ample future research opportunities to delineate the effects of stabilizers on final nanoparticle composition, physical surface area, electrochemical properties, and catalytic performance for OER. However, this work has helped to elucidate aspects of the property-performance relationship of this class of FeNi nanoparticles.

Background

In an increasingly industrialized world, the demand for energy is larger than ever before. Exponential population growth, coupled with continual increases in desired standards of living, has precipitated energy-intensive economies. Since most energy production today continues to be derived from fossil fuels, harmful combustion product gases continue to be added to the atmosphere at alarming rates. Considering the environmental damage of continued emissions, the development of clean energy is essential for sustainable human development.

Many clean energy conversion technologies seek to utilize the chemical storage of energy for later use through oxidation via direct combustion or the use of fuel cells (1). Hydrogen is often considered a promising candidate for energy conversion technologies due to its high specific energy density (2) and low environmental cost, as direct combustion of renewably-produced hydrogen is carbon neutral (1). Additionally, hydrogen is a feedstock for manufacturing ammonia (3), an important component of fertilizer. In these ways, hydrogen has the potential to greatly impact society as related to energy and food security. However, most current means of production for hydrogen fuel are harmful to the environment. The reformation of steam with natural gas and the gasification of coal and other hydrocarbons introduce significant environmental costs associated with air emissions and land use (5). For this reason, more efficient and environmentally-benign production of hydrogen has large implications for the clean energy problem.

OER: A Promising Avenue for Clean Energy

A viable method for clean hydrogen production is splitting water into its component gases, which can be achieved by a variety of processes. Direct water electrolysis, one of these processes, occurs when ample overpotential is applied to an electrochemical cell. Water

electrolysis has been gaining interest as it can be powered by external sources of renewable energy (1). Alkaline water electrolysis has gained considerable attention due to increases in stability and practicality as compared to acidic electrolysis (6). In electrolysis, water is decomposed to molecular hydrogen and oxygen by two half-reactions governing the electron flow, the hydrogen evolution reaction (HER) and the oxygen evolution reaction (OER). HER and OER occur in alkaline electrolyte as represented by Equations 1 and 2 below.

$$2H_2O_{(l)} + 2e^- \rightarrow H_{2\,(g)} + 2OH^-_{(aq)} \qquad E^o = 0 \text{ V vs. RHE} \qquad \text{Eqn. 1 (HER)}$$

$$4OH^-_{(aq)} \rightarrow O_{2\,(g)} + 2H_2O_{(l)} + 4e^- \qquad E^o = 1.223 \text{ V vs. RHE} \qquad \text{Eqn. 2 (OER)}$$

Each of these reactions take place on separate electrodes. HER has been shown to readily occur with high efficiency on a variety of electrocatalysts at the cathode of an electrochemical cell (1). However, OER employs a more complex, multistep, four-electron transfer mechanism that currently requires high overpotentials at the anode for the decomposition of water (1). For this reason, the oxygen evolution half-reaction is more sluggish and controls the overall rate of electrolysis.

Subsequently, while the optimization of water electrolysis represents a potentially cost-effective and environmentally-friendly method for hydrogen fuel production, OER sets a limit on the development and commercial implementation of electrolysis technology (6). For this reason, significant motivation exists to design an optimized catalyst for oxygen evolution.

Why $FeNiO_x$?

Many materials have been found to show considerable activity for oxygen evolution. Nickel, as an abundant metal with intrinsic OER activity, has garnered considerable attention as an essential component of an OER catalyst (7, 8, 9). Nickel oxides have been used for over

a century in battery applications, and their OER activity was discovered somewhat serendipitously (1). Recent work suggests that the most highly active nickel-based catalysts for OER are nickel (oxy)hydroxides that contain iron within their layered structure (2). Trotochaud et al. (9) found that unintentional doping of iron from trace amounts in an electrolyte solution greatly enhanced activity for OER. Smith et al. (10) indicated that the inclusion of iron stabilizes higher oxidation states of nickel, leading to improvements in OER activity. Louie, Bell et al. (11) confirmed that even minimal iron doping into a nickel hydroxide film causes significant enhancement of OER electrochemical performance. Batchellor et al. (12) indicated that the Ni(Fe)OOH system is the fastest known OER catalyst in base electrolyte. This result was true not only for films, but also for nanoparticles. When compared to monometallic iron and nickel nanoparticles, Fe−Ni nanoparticles showed enhanced catalytic activity for OER under alkaline conditions (2). Additionally, Friebel et al. (3) suggested that iron may in fact be the active site of OER, with nickel hydroxide acting as a host lattice. Supporting this proposition, the amount of iron in an iron-nickel bimetallic hydroxide catalyst was found to be a key parameter to control in the optimization of these catalysts for OER performance (4). As the reported findings show, iron and nickel nanoparticles show much potential for prospects in OER catalysis.

Previous Work

Previous work in iron-nickel oxides for OER has been conducted by Dr. Greenlee's research group at the University of Arkansas. Greenlee et al. developed a facile aqueous synthesis method to produce iron-nickel hydroxide ($Fe_xNi_y(OH)_2$) nanoparticles (2, 6). This stabilized-metal-in-solution approach allows for the study of many different parameters, such as composition and morphology. An iron sulfate salt is stabilized with aminotris(methylene

phosphonic acid) (ATMP) while a nickel chloride salt is stabilized with an organic polymer, polyvinylpyrrolidone (PVP). Two distinct, spherical morphologies of nanoparticles (Fe-Ni alloys and Fe@Ni core-shell particles) can be produced, and the starting concentrations of metal precursors dictate the composition of the nanoparticle products (2, 6).

Previous studies suggested that alloy nanoparticles showed more activity, but less stability, than their core-shell counterparts. Other work confirmed that the ratio of Fe:Ni in the alloy nanoparticles plays a critical role in OER performance; an increase in performance was observed with a decrease in the iron content of alloy particles (6). Additionally, previous studies that varied the ratio of nickel metal to PVP stabilizer suggested that, while the amount of stabilizer may play a role in catalyst performance for OER, further experiments are necessary to completely delineate the role of the stabilizer in FeNi nanoparticle catalyst performance (6). Other research with PVP has shown conflicting results, where some have seen improvements while others have seen decline in catalytic performance as the stabilizer to metal ratio increased. PVP most likely increases performance by stabilizing more metals and allowing more incorporation into the nanoparticles, but too much PVP could result in a masking of the catalysts' active sites. These conflicting results suggest that other catalyst parameters, such as surface area, are changed with different nanoparticle stabilizer concentration and compositional ratio.

For this reason, significant motivation exists for continued study and understanding of this class of materials for OER. In particular, it is important to consider not only the catalyst composition and stabilizer concentration, but also an experimental approach to evaluating the electrochemical performance that includes consideration of the electrocatalyst surface area.

Surface Area, ECSA, and Electrocatalysis

Heterogenous catalysis occurs when a chemical reaction takes place on a catalyst with a phase different from the reacting species. These reactions commonly take place at active sites on a catalyst surface. Generally, as the surface area of a heterogenous catalyst increases, so does the overall reaction rate. With more exposed surface area, more active sites are available to participate in reactions, and less mass transfer limitations exist between the two phases participating in the chemical reaction. These factors contribute to a decrease in the activation energy required for the reaction to take place, leading to an overall speeding up of the catalytic process.

Electrocatalysis, which occurs at active sites in electrical contact with electrodes in an electrochemical cell, uses the flow of electrons as the driving force for many heterogenous reactions. A standard electrochemical three-cell setup includes a working electrode, where potential is applied; a counter electrode, to and from which electrons can flow; and a reference electrode, used to measure the potential of the working electrode. Figure 1 below by Bard (13) illustrates a common electrode reaction pathway. In heterogenous electrocatalysis, the reaction rate constant is a function of applied potential. These potential-dependent electron-transfer reactions are called Faradaic processes and cause reduction or oxidation to occur. When an electrode is polarized, current can flow through electrochemical reactions that occur at the electrode surface.

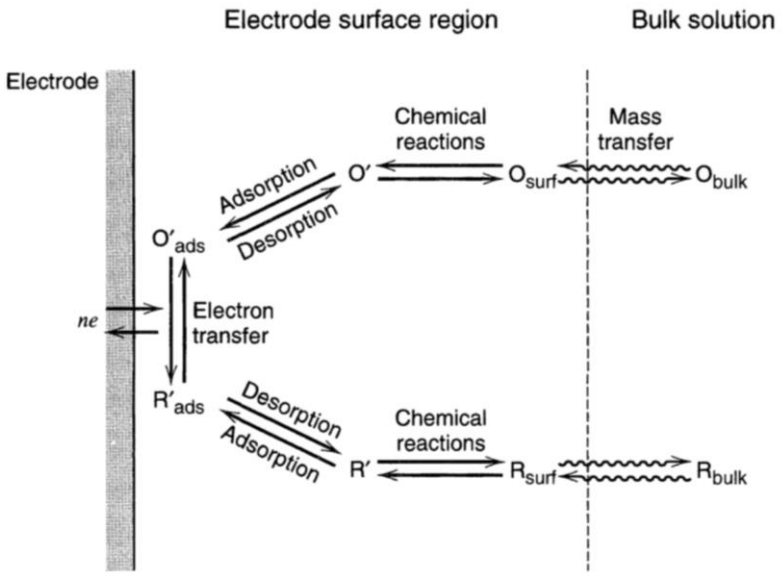

Figure 1. General reaction at an electrode in an electrochemical call (13).

Any potential beyond thermodynamic requirements necessary for a given reaction to take place is deemed the 'overpotential' (13). The overpotential is a function of physical and chemical parameters related to mass transfer and chemical kinetics. The concept is important for electrolysis catalyst research and development, as large overpotentials are associated with inefficient and costly water splitting and hydrogen production processes.

These electron transfer processes at electroactive sites, however, are not the only types of processes that occur at electrodes in an electrolyte solution. In fact, a given electrode-solution interface will show a range of potentials where no charge-transfer reactions occur because such reactions are thermodynamically or kinetically unfavorable (13). These potential regions are dubbed 'non-Faradaic zones' and represent attractive regions for the study of physical and electrochemical properties of electrocatalysts. In these zones, electron transfer is associated primarily with capacitive charging of the electric double-layer than forms in solution, which can tell much about a catalyst's surface structure (14).

It is believed that electrocatalysts with increased electrochemically active surface areas (ECSAs) require lower overpotentials than similar catalysts with smaller ECSAs (13). This ECSA refers to all the electroactive material that is in contact both with reacting species and with electrodes or regions of applied potential. The magnitude of the ECSA is related to the amount of area through which electrons can flow to meet and interact with reactive chemical species. As ECSA increases, so should the reaction rate and therefore the generated charge density at a given overpotential.

These hypotheses have proven to be true for water electrolysis. A plot generated by Bau et al. comparing Tafel activity with values of ECSA found that OER reaction kinetics and overpotential requirements are primarily governed by the ECSA of the electrocatalysts (1). Therefore, significant motivation exists to understand the relationship between various synthesis parameters of these FeNi nanoparticles, such as morphology and metal-to-stabilizer ratio, and their resulting ECSAs.

Double Layers in Electrolyte Solutions

Any charged, conductive material in an electrolyte solution forms a so-called ‘electric double layer’ on the interface between conductor and solution (15). This double layer is composed of an array of charged species and oriented dipoles existing at the metal-solution interface, and its structure can affect the rates of electrode processes (13). The solution side of the double layer is thought to be made up of several "layers." In electrocatalysis, these layers forms when ions and solvent molecules adsorb onto the surface of catalyst or electrodes. Then, electrostatic forces generated from this pseudo-layer accumulation of ions attracts solvated ions of opposite charge, forming the inner and outer Helmhotz planes (IHP and OHP). A schematic of a typical double-layer is shown in Figure 2 below.

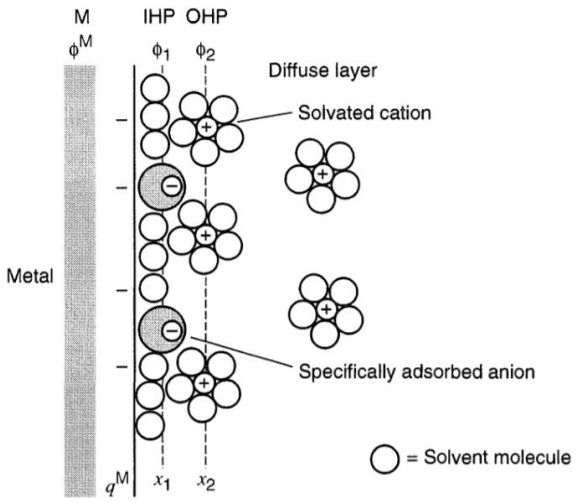

Figure 2. Structure of the electrical double layer (13).

By the formation of a double layer, a thin insulating film is created between two conducting media. When two conductors are separated by an insulator, a capacitor is formed. Therefore, the behavior of the electrode-solution interface is analogous to that of a capacitor (13).

Capacitance, Nickel Redox, and ECSA

As aforementioned, capacitors are formed when two conductors are separated by an insulator. Generally, the magnitude of capacitance of the formed capacitor is a function of potential (13). When a potential is applied across a capacitor, a current (called the charging current) will flow until charge equilibrium is achieved as an excess of electrons on one plate and a deficiency of electrons on the other (13). Analysis of this charging current can quantify the double layer's properties, such as capacitance and ECSA. By varying sweep rates during cyclic voltammetry experiments in a non-Faradaic zone, the capacitance of a conductor-solution interface can be measured as the slope of a scan rate vs. charging current plot (14).

Another requirement for the estimation of capacitance of a certain catalyst material is a conducting catalyst material itself. Without a conductive material-solution interface, a

capacitor between the material and the electrolyte will not form, and only the capacitance of the metal electrode support will be detected by charging current experiments. This fact is significant for the study of FeNi nanoparticles in particular, as nickel oxides are not conductive below the nickel redox peak, which occurs around 0.5 V vs. Hg/HgO. At potentials well below the onset of the OER, Ni is present as α-$Ni(OH)_2$ in the absence of Fe and as a layered double hydroxide structure in the presence of Fe (3). These materials are not conductive. Batchellor et al. concluded that $Ni(OH)_2$ only becomes conductive after oxidation to NiOOH, and that below the nickel redox peak, ions in the electrolyte to polarize directly against the underlying conductive substrate (12). These results suggest that ECSAs measured below the nickel redox peak would be reflective of the ECSA of the underlying electrode support, and not the specific material being studied. For this reason, when studying the capacitance of nickel oxide materials, a potential above the nickel redox peak must be applied to ensure the catalyst material is conductive enough to form a capacitor in solution.

Once the capacitance of a certain electrocatalyst is known, its electrochemically active surface area can be estimated, as reported by McCrory et al. with the following equation (14)

$$\mathrm{ECSA} = \frac{C_{DL}}{C_s} \qquad \text{Eqn. 3}$$

where C_s is the specific capacitance of a certain material as determined by other empirical experiments.

As aforementioned, the scan-rate dependent charging current represents a facile method to measure the capacitance of a double layer in solution. However, because high applied potentials are required for nickel oxides to achieve conductivity, interferences from Faradaic processes limit the scope of charging determination experiments for nickel oxides.

Additionally, capacitance measurements are accurate only for experiments where the overall cell potential does not change very much in a non-Faradaic region (13). For these reasons, another method is required to estimate the capacitance and, in turn, the ECSA of any nickel-based electrocatalysts of interest.

EIS and Equivalent Circuits

Potentiostatic electrical impedance spectroscopy (EIS) provides an alternate route to study the capacitance of electrocatalytic materials. During EIS, a small sinusoidal potential with a wide range of frequencies is applied to the working electrode, and the electrochemical system's response is measured (14). An electrochemical cell can be modeled as an impedance to a small sinusoidal excitation. Therefore, an 'equivalent circuit' of resistors and capacitors that pass current with the same amplitude and phase angle as the real cell under a given excitation should model the cell accurately (13). Because these equivalent circuit elements respond to changes in applied frequency in unique ways, fitting equivalent circuit models to EIS data is useful for the characterization of electrochemical systems. Also, potentiostatic EIS allows the working electrode to be held at a specified potential while experiments are being run. This combination of characterization with the ability to apply potential means that this technique can accurately be used to estimate the capacitance of nickel oxide electrocatalysts.

Frequently, an electrochemical cell is modeled by a modified Randle's circuit, which consists of a solution resistance, a polarization resistance, and a capacitor, as shown in Figure 3 below. For electrochemical applications, electrodes and catalyst materials generally act as imperfect capacitors. As such, when the impedance of an electrochemical system is considered, these imperfect capacitors are generally treated as 'constant phase elements' (CPEs) (15). Additionally, parallel elements are introduced because the total current through

the working interface is the sum of the distinct contributions from the double layer charging and other processes (R_p), like electrode polarization (13). The uncompensated solution resistance (R_u) is inserted as a series element, as all current must pass through the solution resistance (13) and is a function of the electrolyte and electrochemical cell setup (15).

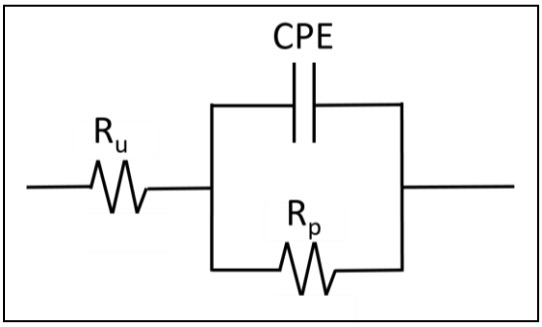

Figure 3. Randles circuit modified with R_u (uncompensated resistance), R_p (polarization resistance), and CPE (constant phase element) used for fitting.

Some other equivalent circuit models include considerations for diffusion, which can create an impedance called a Warburg impedance. This diffusion impedance depends on the frequency of the potential perturbation and is highest at low frequencies, where diffusing species must travel the farthest (15). For this reason, and because a wide range of frequencies are employed, the modified circuit in Figure 3 models the electrochemical cell accurately enough for comparison of capacitances between electrocatalysts despite constraints from diffusion.

Methods

By systematically varying two synthesis parameters, four different nanoparticles were synthesized. Previous work by Greenlee and Acharya (6) suggested that the nominal 1:5 Fe:Ni alloy nanoparticles resulted in the highest activity for OER, so this compositional ratio of metals was kept constant for all materials. This previous study also looked at the effect of the organic stabilizing ligand polyvinylpyrrolidone (PVP) on nanocatalyst performance and found that increased ratios of PVP resulted in increased activity for OER. As a result, when looking at the effect of morphology, a nominal ratio of 1:0.005 of Ni:PVP was kept constant for all synthesized nanoparticles. As delineating the role of PVP on the effect of synthesized nanoparticles remains a design constraint, three different mass ratios of Ni:PVP were used in synthesis for this study, namely 1:0.001, 1:0.005, and 1:0.010, of nanoparticles with alloy morphology for comparison. The following table summarizes the suite of nanomaterials synthesized for this study.

Table 1. Summary of Varied Synthesis Parameters

Name	Fe:Ni Ratio	Morphology	Ni:PVP Ratio
CS (core-shell)	1:5	Core-shell	1:0.005
A1 (low, alloy)	1:5	Alloy	1:0.001
A2 (medium, alloy)	1:5	Alloy	1:0.005
A3 (high, alloy)**	1:5	Alloy	1:0.010

***A3 was made in later rounds of synthesis; few tests were successfully run with this material.*

Materials

ACS grade chemicals were purchased from commercial vendors. Iron sulfate heptahydrate ($FeSO_4*7H_2O$), nickel chloride hexahydrate ($NiCl_2*6H_2O$), sodium borohydride ($NaBH_4$), methanol, Nafion®, aminotris(methylene phosphonic acid) (ATMP), and polyvinylpyrrolidone (MW = 40,000 g/mol) (PVP40000) were used without any alteration.

Potassium hydroxide (KOH) was also purchased from a commercial vendor, and purification of 1 M KOH solutions was applied before use (9). A Millipore Milli-Q® Integral water purification system in the lab supplied ultrapure water.

Synthesis of Nanoparticles

All nanoparticles were synthesized under atmospheric pressure and room temperature. 18.2 MΩ H_2O was used as the solvent for all the solutions. For alloy nanoparticles (NPs), $FeSO_4*7H_2O$ and ATMP were added and hand-mixed together at a molar ratio of Fe:ATMP = 1:0.05. Independently, $NiCl_2*6H_2O$ and PVP40000 were hand-mixed together. For A1, A2, and A3, the molar ratios of nickel to PVP40000 used were Ni:PVP = 1:0.001, Ni:PVP = 1:0.005 and Ni:PVP = 1:0.01, respectively. The mixture of iron salt plus ATMP and the mixture of nickel salt plus PVP were then added to a three-necked round bottom flask. The contents of the flask underwent argon bubbling for 15 minutes while stirred on an orbital shaker at 100 rpm. A $NaBH_4$ solution was then added dropwise with a syringe to chemically reduce the metal precursors into NPs. The ratio of metal to borohydride was mol metal:mol $NaBH_4$ = 1:2.2. Excess $NaBH_4$ accounts for side reactions that occur between water molecules and borohydride (16). The flask was placed under vacuum for 15 minutes on an orbital shaker and rotated at 100 rpm. The vacuum removes the hydrogen gas formed as a byproduct of the reaction between $NaBH_4$ and the metal precursors. After the vacuuming process, the NP solution was transferred to a 50 mL centrifuge tube and centrifuged. The supernatant was decanted, and the NPs were re-suspended in methanol. Fe@Ni core-shell nanoparticles were synthesized in a similar fashion by first reducing iron to form iron nanoparticles and then introducing the nickel-stabilizer mixture (mol Ni:mol PVP = 1:0.005), which coats each iron

nanoparticle by galvanic replacement (2). This synthesis technique is summarized in Figure 4 below. A theoretical basis of 1 g/L of Fe was used in synthesis calculations for all three NPs.

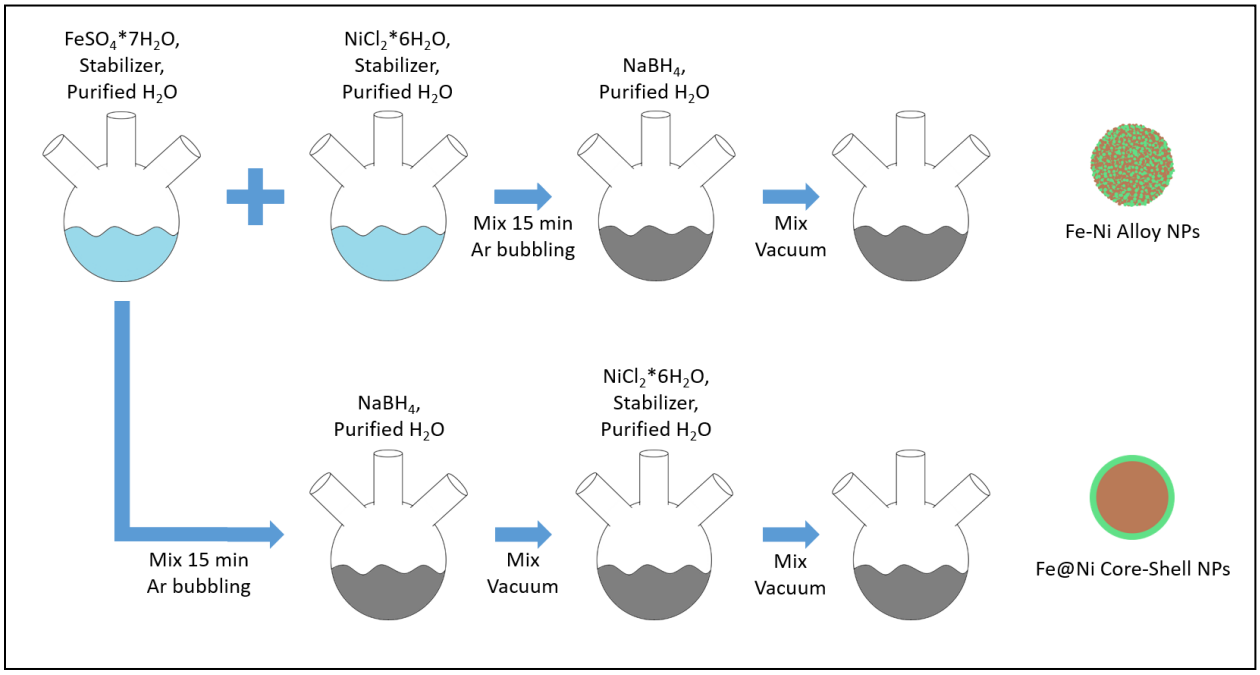

Figure 4. Schematic of alloy and core-shell FeNi NP synthesis.

ICP-MS

Inductively couple plasma mass spectrometry (ICP-MS) was employed for determination of concentrations of synthesized nanoparticle solutions. A procedure developed by Ryan Manso, a graduate student at the University of Arkansas, was followed. A standard curve of both Fe and Ni metal was prepared by dilutions of known standards. Aliquots each nanomaterial solution produced were dried in a vacuum oven then digested in concentrated HNO_3 before being diluted by a factor of 10,000. These dilute, digested samples were then sent to an external characterization lab for spectrometry and analysis.

Physical Surface Area Measurements

BET analysis was used to calculate the physical surface area of each material. NP solutions were centrifuged, decanted, and placed under a fume hood to air dry overnight. Residual adsorbates were removed by degassing for 21 hours at 120°C. These conditions were selected in correspondence with TGA data previously recorded for materials with similar metal-ligand interactions (17). A nitrogen adsorption isotherm was measured at 77 K and multi-point BET analysis was performed with a Quantachrome Autosorb-iQ^{TM}.

Electrochemical Setup

Measurements were performed with potentiostats (Gamry Reference 3000 for EIS and WaveNow for voltammetry) in a stationary three-electrode cell setup. A glassy carbon (GC) electrode (5mm, Pine) was used as the working electrode; a graphite rod was used as the counter electrode; and Hg/HgO was used as the reference electrode. The electrolyte solution used was purified 1M KOH and had a pH of 14. The purification process for KOH was done by following a procedure outlined in the literature (9).

Electrochemical Measurements

Two electrochemical methods—potentiostatic electrochemical impedance spectroscopy (EIS) and scan-rate dependent charging current voltammetry—can be used to calculate ECSA. In this study, only EIS was completed. NPs were mixed with an ionomer (Nafion®) at a mass ratio of 30:1 (g NP:g Nafion) to form a methanol-based ink. The catalyst was applied to the glassy carbon working electrode at a mass loading of around 500 $\mu g/cm^2$ by the dropcasting method. For these loadings, a rough estimate of the synthesized nanoparticle concentration was made by drying and weighing an aliquot of nanoparticle samples. Impedance spectra were

measured at two different potentials: 0 V and 0.52 V vs. Hg/HgO as employed by Batchellor et al (12). The amplitude of the applied sinusoidal wave was 10 mV, and its frequency range was from 0.1 Hz to 100 KHz.

Although scan-rate spectra were not gathered as a part of this study due to time constraints, this method for measuring the C_{DL} will be an integral part of a continuation of this research in the future. Voltammetric scan-rate spectra will be measured in two potential windows, from -0.05 V to 0.05 V and from 0.45 V to 0.55 V vs. Hg/HgO, with scan rates varying from 0.2 mV/s to 800 mV/s. The slope of a linear plot of sweep-rate vs. charging current quantifies the capacitance of the double layer, which can be related to the ECSA (14).

The OER performance of each material was evaluated with cyclic voltammetry in the potential range of 0 – 0.8 V vs Hg/HgO. Each material was applied to the working electrode at a mass loading of around 50 $\mu g/cm^2$ by dropcasting. These loadings were determined by the theoretical amount of iron in the final nanoparticle solutions, based on initial synthesis calculations. The overpotential of each catalyst was determined. By using the theoretical OER potential (E_o = 1.23 V vs. RHE), the potential associated with a measured current density of 10 mA/cm^2 of electrode surface area was corrected for comparison with other experimental setups and results.

Additionally, as part of the continuation of this project, the nickel redox peaks around 0.5 V vs. Hg/HgO that occur during cylic voltammetry will be integrated. By assuming one electron transfer for each nickel atom during redox (12), this peak integration will help to verify mass loadings and to normalize activity to the amount of nanoparticles on the electrode surface. Furthermore, comparing the results from redox peak integration with the results from ICP-MS will show whether or not all nickel atoms applied to the electrode are participating in nickel

redox, and, subsequently, are electrochemically active. Some nickel atoms in the bulk of the nanomaterial might be ‘shielded’ from electroactivity by other atoms on the actual exposed and wetted surface of the nanoparticle. In this way, coupling ICP-MS with redox peak integration can elucidate whether these FeNi nanoparticles exhibit bulk activity.

Results and Discussion

Overall, the results obtained suggest that lower amounts of PVP lead to a reduced surface area, most likely due to less nanoparticle stability in solution and more coalescence of individual particles. Also, there could possibly exist a direct relationship between physical surface area and ECSA of the nanocatalysts, but further research is needed to verify whether this trend is statistically significant. Additional work is required to delineate the effects of metal-to-stabilizer ratio and iron-to-nickel ratio on OER performance, as these two parameters seem to be intertwined.

BET results

Only materials A1, A2, and CS were analyzed with the Quantachrome Autosorb-iQTM. Through BET analysis of nitrogen physisorption measurements for physical surface area (Figure 5), A2 was found to have the largest surface area of the materials studied at 96.0 m^2/g, followed by CS, which had a surface area of 88.1 m^2/g. A1 had the lowest measured surface area of the three tested nanoparticle materials with a value of 54.5 m^2/g.

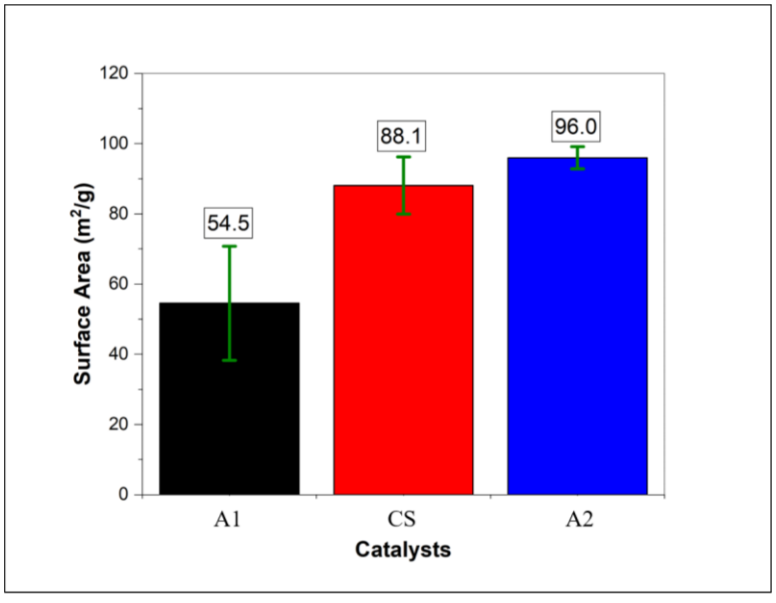

Figure 5. Physical surface area as measured by BET.

A1 nanoparticles were synthesized with the lowest amount of PVP (Ni:PVP = 1:0.001) among the three nanocatalysts. In contrast, both CS and A2 nanoparticles were synthesized with a ratio of Ni:PVP = 1:0.005. The lower amount of PVP used during A1 nanoparticle synthesis appears to have resulted in a significant decrease in the measured surface area. This decrease in measured surface area is possibly the result of increased agglomeration of the nanoparticles and therefore a reduction in the physically accessible surface area for nitrogen adsorption. In addition, the A1 nanoparticles may have a larger average particle diameter, which would reduce the surface area per unit mass. The ratio of PVP ligand stabilizer to metal precursor is known to impact both nanoparticle size and nanoparticle agglomeration in nanoparticle synthesis, and both effects need to be further investigated.

At the higher PVP concentration tested, both A2 and CS nanoparticles resulted in increased measured surface area compared to A1. Interestingly, the measured surface area of the HA nanoparticles is slightly larger than that of the CS nanoparticles. Again, differences in particle diameter may contribute to this difference. However, when comparing alloy with core-shell particles, the incomplete deposition of the nickel precursor may be the major contributor to a lower measured surface area for CS nanoparticles. In Candelaria et al. (2), Fe@Ni core-shell nanoparticles synthesized at a theoretical precursor composition of Fe:Ni = 1:1 were experimentally determined to contain a bulk composition of Fe:Ni = 3.2:1. These results, along with un-reported measurements of remaining nickel salt precursor in the decanted nanoparticle synthesis supernatant, demonstrate that only a portion of the nickel displaces iron metal atoms at the iron nanoparticle surface during core-shell synthesis. This phenomenon may also result in a lower amount of PVP deposition on the surface, causing differences in both nanoparticle size and nanoparticle agglomeration between A2 and CS.

Overall, the relationship between measured physical surface area and nanoparticle synthesis parameters is important to understand. Further investigation, such as the use of nanoscale microscopy for particle diameter estimates, will explore delineation of the roles of nanoparticle size, nanoparticle agglomeration, and nanoparticle morphology.

Impedance spectra

Potentiostatic EIS was run on the same three materials as above – A1, A2, and CS. Impedance spectra were fit to a modified Randles circuit as shown in Figure 3. A pure capacitor was replaced with a constant phase element (CPE) as employed by McCrory et al. (14).

The capacitance of the double layer formed in solution of each material was calculated using Equation 3 (18). Modern EIS analysis uses a computer to find the model parameters that cause the best agreement between a model's impedance spectrum and a measured spectrum. A non-linear least squares fitting (NLLS) algorithm is used (15).

$$C_{DL} = \frac{(Y_0 * R_p)^{\left(\frac{1}{\alpha}\right)}}{R_p} \quad \text{Eqn. 3}$$

C_{DL} is the capacitance of the double layer (F), Y_0 is a parameter that relates to the magnitude of capacity ($S*s^{\alpha}$), R_p is the polarization resistance connected in parallel with the CPE, and α is a dimensionless fit parameter that relates to deviations from a true capacitor. Nyquist plots, which graph imaginary values of impedance against the real values of impedance at a given frequency, were generated after multiple rounds of EIS, and these spectra are summarized in Figure 6 below.

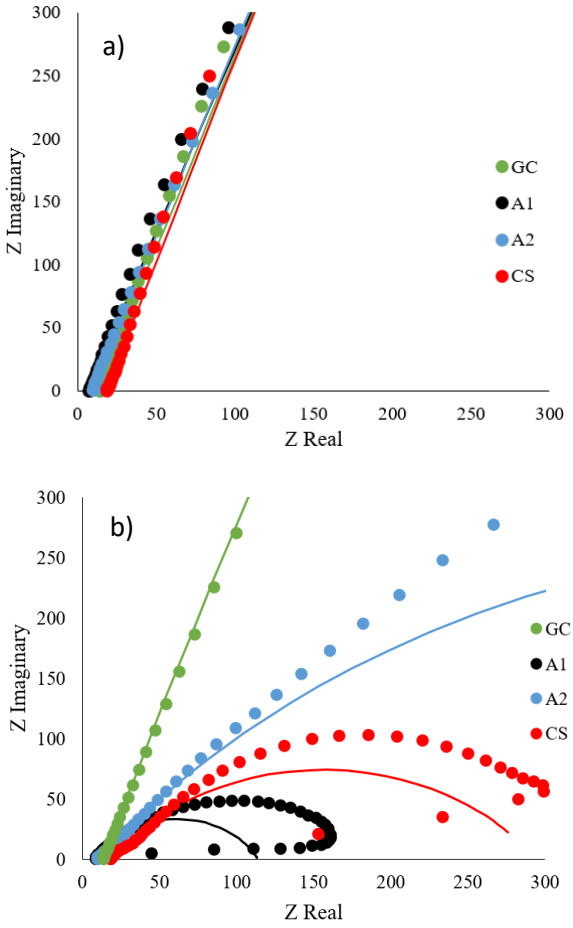

Figure 6. Nyquist plots with CPE fits taken at a) 0 V and b) 0.52 V vs. Hg/HgO.

As is evident by the above plots, most materials showed similar impedance spectra at 0 V vs. Hg/HgO. However, while the GC electrode's impedance spectra was relatively unchanged at 0.52 V as compared to 0 V vs. Hg/HgO, all the nanoparticles exhibited very different impedance spectra at the higher applied potential. The solid lines shown in Figure 6 above represent the modified Randle's fits generated by Gamry's Echem Analyst software and were used to estimate values of C_{DL} for each material.

However, these fits deviate from actual spectra at higher values of impedance. This deviation suggests the equivalent circuit model employed for fitting is not a completely accurate model for all the processes occurring at the electrode. At this higher potential,

faradaic processes can begin to occur, so inclusion of a charge-transfer resistance or a Warburg impedance for diffusion might have resulted in a more accurate model and fit. Nonetheless, for this scope of this project, the modified Randle's circuit described above is assumed to be accurate enough for analysis and comparison between materials.

The ECSA can be determined from the capacitance of the double layer by normalizing C_{DL} with the specific capacitance (C_s). The measured ECSA of a clean GC electrode was calculated to be approximately 1.6 cm^2 and 0.9 cm^2 at 0 V and 0.52 V vs. Hg/HgO, respectively. The capacitance of a single Ni(Fe)OOH nanosheet has previously been reported to be 0.04 mF/cm^2 (4), and this value of C_s was used to find the ECSA of the nanoparticles. ECSA values of the blank electrode and three nanocatalysts are plotted in Figure 7 below.

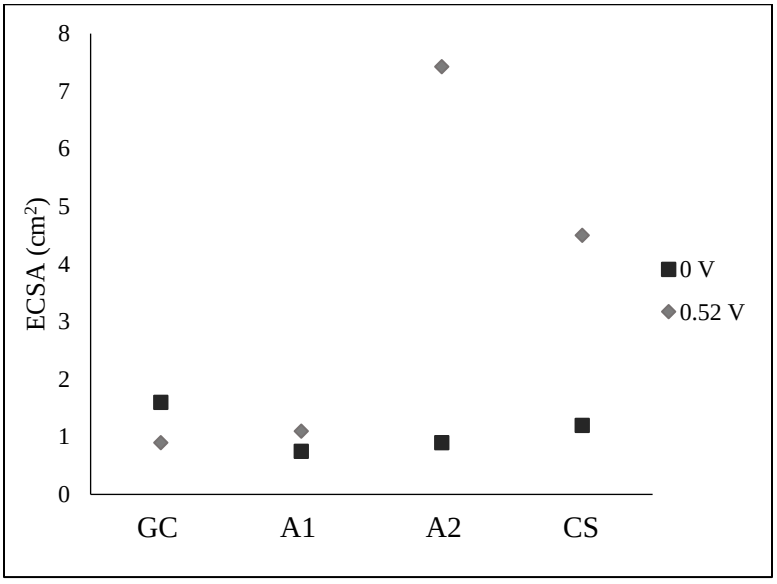

Figure 7. ECSA measurements of electrode and nanoparticles at 0 V and at 0.52 V vs. Hg/HgO.

At 0 V vs Hg/HgO, ECSA values of the three nanoparticles were quite similar and were within the range of 0.5 – 1.2 cm^2. These results closely match the ECSA obtained for the clean GC electrode. At 0.52 V vs Hg/HgO, the measured ECSA for A1 nanoparticles was not

significantly greater than the ECSA acquired at 0 V. However, for A2 and CS nanoparticles, ECSA values obtained above the nickel redox peak at 0.52 V vs. Hg/HgO increased by approximately 8 and 4 times, respectively, above those acquired at 0 V.

These results are consistent with the findings of Batchellor et al. (12). Below the nickel redox peak, only the GC electrode is conductive. Therefore, the working electrode was the only electrochemically active area detected by the double-layer capacitance method when the applied potential is 0 V vs. Hg/HgO. Above the redox peak at 0.52 V vs. Hg/HgO, A2 and CS showed large increases in the measured ECSA. These results are most likely due to the increase in conductivity of nickel oxyhydroxide over nickel hydroxide. Therefore, measurements taken at 0.52 V vs. Hg/HgO are more likely to be reflective of the true ECSA of the nanoparticles.

Because A1 showed only a minimal increase in ECSA at the higher applied potential, one of two conclusions can be drawn: either nanoparticles with less PVP have much smaller values of true ECSA, or the nanoparticles with a lower PVP ratio were not conductive at the higher applied potential. The latter might be the case if lacking sufficient nickel redox to achieve conductivity. This lack in conductivity for A1 at 0.52 V could be due to a smaller amount of nickel incorporation into the alloy nanoparticles, or to a higher redox potential requirement because of some other factor. Due to the similar composition of these three nanoparticles, however, it is more likely that A1 was indeed conductive at 0.52 V vs. Hg/HgO. Assuming A1 was conductive at the higher potential, these data suggest that nanoparticles with higher ratios of PVP result have higher ECSAs. However, additional work focused on testing higher ratios of PVP is necessary to validate this trend.

Figure 8 below shows ECSA plotted as a function of BET physical surface area. As before, only three of the four synthesized materials are reported in this plot (A1, A2, CS). This plot suggests a positive correlation between physical surface area and electrochemically active surface area. This relationship could be valid, as more exposed surface area could generate more electrochemical area and more electroactive sites.

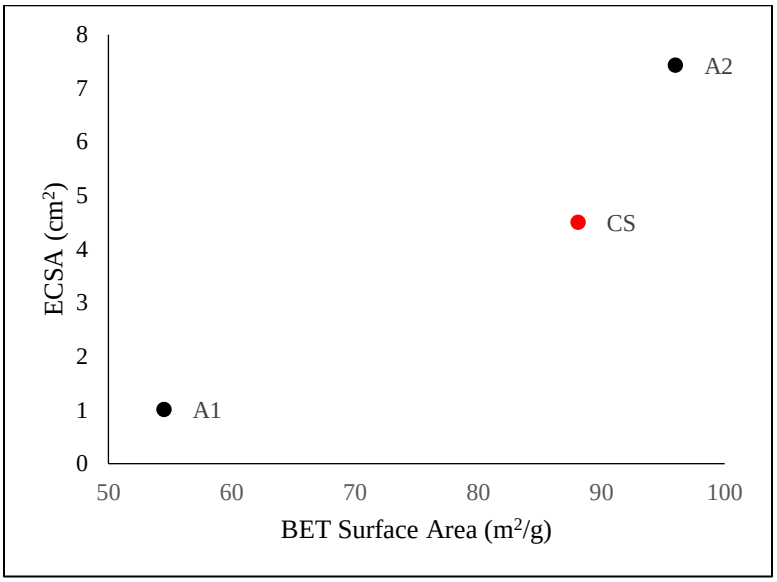

Figure 8: ECSA at 0.52 V vs. Hg/HgO and BET surface area for three nanomaterials.

However, since this dataset is limited, future characterization of multiple materials with different compositions is necessary to truly define a relationship between ECSA and physical surface area.

Performance data

Figure 9 below summarizes the background-subtracted data obtained from CV experiments on materials A1, A2, and CS. The dashed line in the plot represents the benchmark current density of 10 mA/cm^2 used for comparing materials.

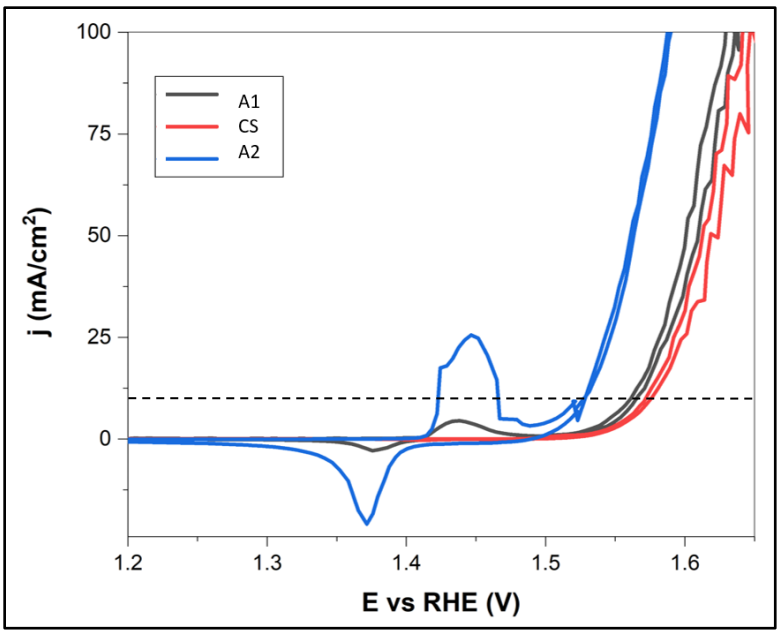

Figure 9: Cyclic voltammograms obtained for A1, A2, and CS used to evaluate performance (Acharya et al. in submission).

Overpotentials of each catalyst were taken as the first potentials past nickel redox that achieved the benchmark current density. The overpotentials of A1, A2, and CS were determined to be 331 mV, 298 mV, and 341 mV, respectively. These overpotential values suggest that the alloy morphology performs better for OER than the core-shell morphology, as the CS material had the highest overpotential of all materials tested. Performance data also suggest that the nanoparticle with a higher PVP ratio was a better catalyst for OER over its low-PVP counterpart. Comparing these performance data to surface area data as in Figure 10 below suggests that neither morphology nor ECSA alone govern electrocatalyst performance. Instead, it seems that morphology has a larger impact. While A2 and CS had the same amount of PVP in synthesis and similar values of ECSA, A2 showed large improvements in OER performance over CS. Also, though the ECSA of A1 was much less than the ECSA of CS, A1 had a slightly smaller overpotential than CS.

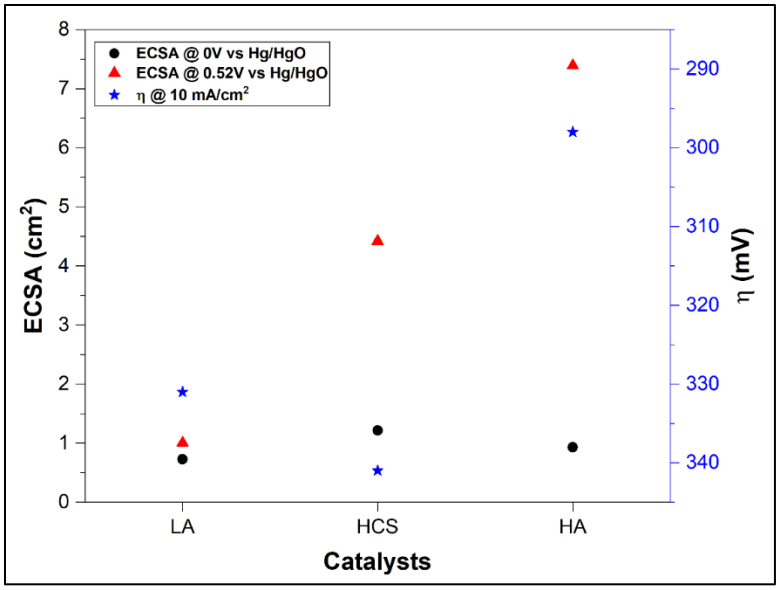

Figure 10: Calculated ECSA values for each material at 0V and at 0.52V vs. Hg/HgO, as well as measured overpotential (η).

These combined datasets suggest that morphology is a primary dictator of catalyst performance when comparing alloys against core-shell nanoparticles, and that, within the alloy morphology itself, ECSA governs OER performance.

ICP results

The standard curves that were prepared for iron and nickel ICP spectroscopy are presented in Figure 11 below.

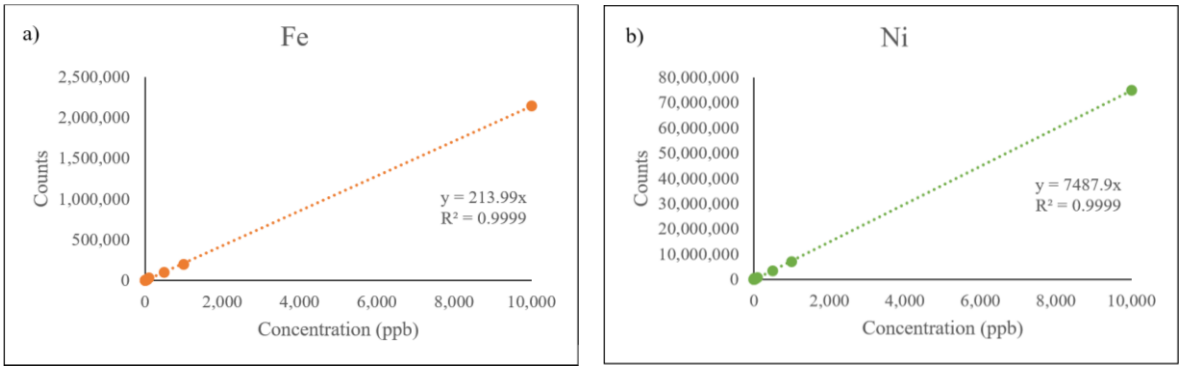

Figure 11: ICP-MS standards with fits: a) Fe and b) Ni.

The table below summarizes the linear fits obtained from standard curves.

Table 2. Linear fits to standards.

Standard Curve		
	Rsq	Slope
Fe	0.9999	213.99
Ni	0.9999	7487.93

These fits were correlated with the counts obtained from ICP-MS data to determine the concentration of each synthesized sample as summarized by Tables 3, 4, and 5 below. Samples are named in the tables below such that "A1 10" refers to the 10,000x diluted aliquot, while "A1" refers to the corrected concentration of original A1 sample.

Tables 3, 4, and 5. Determination of concentration of synthesized samples.

Counts		
	Fe	Ni
A1 10	9996.04	792621.62
A2 10	17029.68	2237086.78
A3 10	22995.24	3199118.28
CS 10	9749.84	105980.01

Correlation		
	Fe (ppb)	Ni (ppb)
A1 10	34.69	105.25
A2 10	67.56	298.16
A3 10	95.44	426.63
CS 10	33.54	13.55

Concentration		
	Fe (g/L)	Ni (g/L)
A1	0.35	1.05
A2	0.68	2.98
A3	0.95	4.27
CS	0.34	0.14

Because a blank was used for calibration during ICP-MS and since all nanoparticles are washed in methanol and decanted after synthesis, all the metals in the digested aliquots are assumed to have been incorporated into the nanoparticle itself (and not just soluble metals in solution). With this assumption, the concentrations determined above are assumed to be reflective of the relative compositions of the synthesized nanoparticles. The following plots summarize how the nanoparticle metal composition is effected by varying the ratio of Ni:PVP.

While only composed of three data points, Figure 12 implies a clear trend of increased incorporation of both nickel and iron into the alloy nanoparticles. These increased concentrations (and assumedly nanoparticle metal incorporations) occurred despite having every synthesis parameter identical except for the mass of PVP added.

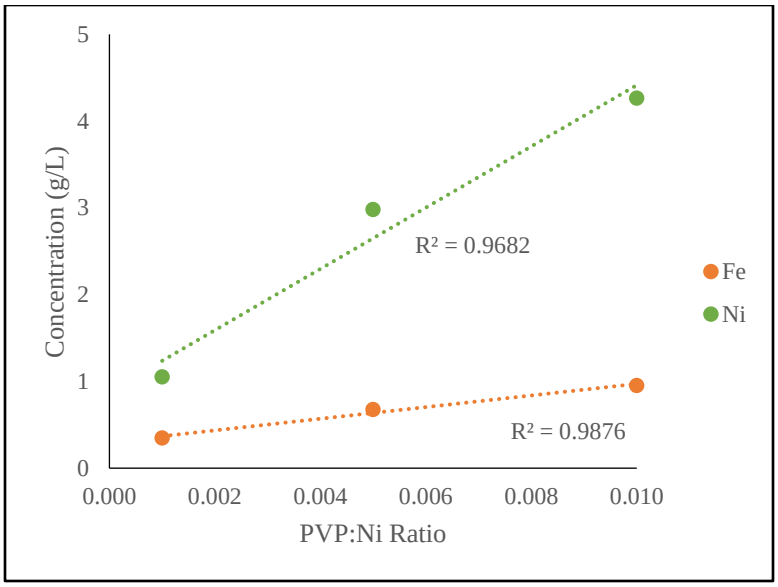

Figure 12. Concentrations of metals in alloy NP solutions as function of PVP:Ni ratio.

The masses of precursors used in synthesis were calculated using a basis of 1 g/L of iron in the final nanoparticles. However, only the alloy nanoparticles made with the most PVP resulted in a final iron concentration near this theoretical value. Because more PVP caused increased iron incorporation, PVP can also be assumed to act as a stabilizing agent for iron in solution. These results could suggest that the stabilization provided by PVP allows for more metal atoms, both nickel and iron alike, to be integrated into the alloy nanoparticles. If all the iron metal in solution is successfully stabilized by ATMP, then the addition of PVP should not increase iron incorporation in the nanoparticle products. This result could suggest that a higher ATMP:Fe ratio is necessary for the complete stabilization of iron in solution.

Figure 13 below shows the nickel to iron ratio as a function of PVP to nickel ratio. While all metal precursor ratios were the same, this plot shows that none of the nanoparticles were actually composed of a theoretical ratio of Fe:Ni = 1:5. A2 and A3 have similar metal ratios with nearly 4.5x as much nickel as iron, while A1, which had much less PVP, had only about

3x as much nickel as iron. This fact suggests that the theoretical metal ratio is approached with the addition of more PVP for alloy nanoparticles.

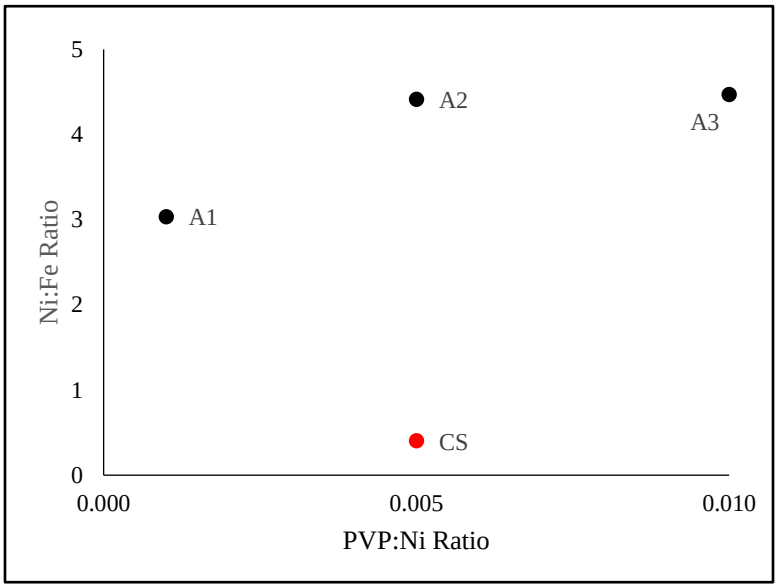

Figure 13. Nickel to iron molar ratio of all synthesized materials as a function of PVP:Ni ratio.

The core-shell nanoparticle CS is not displayed on Figures 12 above but had an iron concentration of 0.34 g/L (theoretical: 1 g/L), a nickel concentration of 0.14 g/L (theoretical: 5.3 g/L), and an iron to nickel ratio of 2.4 (theoretical: 0.2). Due to the nature of core-shell synthesis, the PVP stabilizer never contacts iron metals in solution before they have been reduced to nanoparticles by borohydride. Perhaps the low iron concentration is again a result of a deficit in ATMP stabilizer ratio.

As previously reported by Candelaria et al., the metal ratio suggests that a significant amount of nickel was decanted off and not incorporated into the nanoparticles (2). Additional core-shell particles with different PVP ratios should be studied to see the effect of PVP stabilization on the incorporation of nickel into the core-shell nanoparticle synthesis.

Future Studies

There are ample opportunities for future studies as related to this work. First and foremost, EIS measurements should be coupled with ICP results and repeated for all nanoparticle samples. This coupling will insure accurate loading on the electrode and would allow for ECSA normalization to nanoparticle mass. Additionally, other nanoparticles with different ratios of both PVP and ATMP should be synthesized and tested to verify trends that have been presented in this report. A rotating-disk electrode setup should be employed during EIS testing to limit diffusion and cut down on any Warburg impedance present at high frequencies. In relation to RDEs, the ionomer to nanoparticle ratio should be manipulated to prevent nanoparticles from detaching from the working electrode. Additionally, changing ionomer and electrode combinations should be employed to replace Nafion and glassy carbon with an experimental ionomer on a gold electrode, which has been known to show better activity for OER (21). If possible, the scan-rate dependent method for measuring capacitance should also be employed as a verification of the potentiostatic EIS method. Additionally, when changing synthesis parameters, both the mass ratios and the concentrations employed should be controlled, as concentration of reactants could affect reaction rates and kinetics during synthesis. Lastly, more intensive characterization techniques, such as microscopy, XPS, and XRD could be employed for better understanding of the nanoparticle structures.

Conclusion

The results from this study suggest that PVP has a significant effect on nanoparticle performance through the functions of composition and of physical and electroactive surface areas. Increasing ratios of PVP resulted in metal incorporation that approached expected theoretical values and in larger BET surface areas. Additionally, nanoparticle alloys with higher PVP ratios

exhibited larger double-layer capacitances and ECSAs, which were correlated with increases in performance. Surface area increases are expected to be associated with changes in particle diameter or in agglomeration through the stabilizing function of the PVP ligand. Though significant room for future studies exists, this surface area study contributed to an elucidation of the structure-property-performance relationship of FeNi nanoparticles and will serve as the basis for continued research of this class of materials.

Acknowledgements

The author would like to thank Dr. Lauren Greenlee for her mentorship throughout the undergraduate research process; Prashant Acharya for his collaboration and assistance in experimental setup and data acquisition; Mojtaba Abolhassani for his help with BET measurements; and Sergio Bakovic and Ryan Manso for their guidance through ICP-MS analysis. Additionally, this work would not have been possible without the generosity of the Honors College at the University of Arkansas, as this research was funded by an Honors College Research Grant.

References

1. J.A. Bau, E.J. Luber, and J.M. Buriak. "Oxygen Evolution Catalyzed by Nickel=Iron Oxide Nanocrystals with a Nonequilibrium Phase". ACS Applied Materials & Interfaces (2015) 7:35, 19755-19763. DOI: 10.1021/acsami.5b05594

2. S. Candelaria, N.M. Bedford, A.R. Showalter, S. Pylypenko, B.A. Bunker, S. Lee, B. Reinhart, Y. Ren, S.P. Ertem, E.B. Coughlin, N.A. Sather, J.L. Horan, A.M. Herring, L.F. Greenlee. "Multi-Component Fe-Ni Hydroxide Nanocatalyst for Oxygen Evolution and Methanol Oxidation Reactions under Alkaline Conditions". ACS Catalysis (2017) 7, 365-379. DOI: 10.1021/acscatal.6b02552

3. D. Friebel, M.W. Louie, K.E. Sanwald, Y. Cai, A.M. Wise, M.J. Cheng, D. Sokaras, T.C. Weng, R. Alonso-Mori, R.C. Davis, J.R. Bargar, J.K. Nørskov, A. Nilsson, and A.T. Bell. "Identification of Highly Active Fe Sites in (Ni,Fe)OOH for Electrocatalytic Water Splitting". J. Am. Chem. Soc. (2015) 137:3, 1305-1313. DOI: 10.1021/ja511559d

4. S. Klaus, M.W. Louie, L. Trotochaud, and A.T. Bell. "Role of Catalyst Preparation on the Electrocatalytic Activity of Ni1–xFexOOH for the Oxygen Evolution Reaction". J. Phys. Chem. C (2015) 119:32, 18303-18316. DOI: 10.1021/acs.jpcc.5b04776

5. A. Herzog and M. Tatsutani. "A Hydrogen Future? An Economic and Environmental Assessment of Hydrogen Production Pathways". Natural Resources Defense Council Issue Paper (2005). Retrieved from https://www.nrdc.org/sites/default/files/hydrogen.pdf

6. L.F. Greenlee, P. Acharya, and Z. Nelson. "Compositional Optimization of Alloy FexNiy(OH)2 Nanoparticles for Alkaline Electrochemical Oxygen Evolution". ECS Transactions (2017) 77, 25-38. DOI: 10.1149/07709.0025ecst

7. D.A. Corrigan. "The Catalysis of the Oxygen Evolution Reaction by Iron Impurities in Thin Film Nickel Oxide Electrodes". J. Echem. Soc. (1987) 134:2, 377-384. DOI: 10.1149/1.2100463

8. J. Qi, W. Zhang, R. Xiang, K. Liu, H. Wang, M. Chen, Y. Han, and R. Cao. "Porous Nickel-Iron Oxide as a Highly Efficient Electrocatalyst for Oxygen Evolution Reaction". Adv. Science (2015) 2:10. DOI: 10.1002/advs.201500199

9. L. Trotochaud, S.L. Young, J.K. Ranney, and S.W. Boettcher. "Nickel-Iron Oxyhydroxide Oxygen-Evolution Electrocatalysts: The Role of Intentional and Incidental Iron Incorporation". J. Am. Chem. Soc. (2014) 136:18, 6744-6753. DOI: 10.1021/ja502379c

10. R.D.L. Smith, M.S. Prevot, R.D. Fagan, S. Trudel, and C.P. Berlinguette. "Water Oxidation Catalysis: Electrocatalytic Response to Metal Stoichiometry in Amorphous Metal Oxide Films Containing Iron, Cobalt, and Nickel". J. Am. Chem. Soc. (2013) 135, 11580-11586. DOI: 10.1021/ja403102j

11. M.W. Louie and A.T. Bell. “An Investifation of Thin-Film Ni-Fe Oxide Catalysts for the Electrochemical Evolution of Oxygen”. J. Am. Chem. Soc. (2013) 135:33, 12329-12337. DOI: 10.1021/ja405351s

12. A.S. Batchellor and S.W. Boettcher. “Pulse-Electrodeposited Ni–Fe (Oxy)hydroxide Oxygen Evolution Electrocatalysts with High Geometric and Intrinsic Activities at Large Mass Loadings”. ACS Catal. (2015) 5:11, 6680-6689. DOI: 10.1021/acscatal.5b01551

13. A.J. Bard and L.R. Faulkner. Electrochemical Methods: Fundamentals and Applications. New York: Wiley, 2001. 2nd ed. Print.

14. C.C.L. McCrory, S. Jung, J.C. Peters, and T.F. Jaramillo. “Benchmarking Heterogeneous Electrocatalysts for the Oxygen Evolution Reaction”. J. Am. Chem. Soc. (2013) 135:45, 16977-16987. DOI: 10.1021/ja407115p

15. Gamry Instruments. “Basics of Electrochemical Impedance Spectroscopy”. April 17, 2018. Retrieved from https://www.gamry.com/application-notes/EIS/basics-of-electrochemical-impedance-spectroscopy/

16. N. Goldstein and L.F. Greenlee. “Influence of synthesis parameters on iron nanoparticle size and zeta potential”. J. Nanoparticle Research (2012) 14:760. DOI: 10.1007/s11051-012-0760-5

17. S.K. Karna, S.R. Mishra, E. Gunapala, I. Dubenko, G.K. Marasinghe, and N. Ali. “Synthesis and Characterization of FeNi/Polymer Nanocomposites”. J. Nanoscience and Nanotechnology (2010) 10:9, 5879-5884. DOI: 10.1166/jnn.2010.3106

18. V.D. Jovic. “Determination of the correct value of Cdl from the impedance results fitted by the commercially available software”. Res. Solut. Resourc. Gamry Application Note (2003). Retrieved from https://www.gamry.com/assets/Application-Notes/Determination-of-Double-Layer-Capacitance-from-a-CPE.pdf

19. K.M. Krause, M.T. Taschuk, K.D. Harris, D.A. Rider, N.G. Wakefield, J.C. Sit, J.M. Buriak, M. Thommes, and M.J Brett. “Surface Area Characterization of Obliquely Deposited Metal Oxide Nanostructured Thin Films”. Langmuir (2010) 26:6, 4368-4376. DOI: 10.1021/la903444e

20. E. Fabbri, A. Habereder, K. Waltar, R. Kötz and T. J. Schmidt. “Developments and perspectives of oxide-based catalysts for the oxygen evolution reaction”. Catal. Sci. Technol. (2014) 4, 3800-3821. DOI: 10.1039/c4cy00669k

21. M.B. Stevens, C.D.M. Trang, L.J. Enman, J. Deng, and S.W. Boettcher. “Reactive Fe-Sites in Ni/Fe (Oxy)hydroxide Are Responsible for Exceptional Oxygen Electrocatalysis Activity”. J. Am. Chem. Soc. (2017) 139, 11361-11364. DOI: 10.1021/jacs.7b07117